Chemistry–A European Journal
Research Article
doi.org/10.1002/chem.202303619
Chemistry Europe
European Chemical Societies Publishing
www.chemeurj.org

Autocatalysis in Eschenmoser Coupling Reactions

Quentin Duez[+],*[a] Lukáš Marek[+],[b] Jiří Váňa,[b] Jiří Hanusek,*[b] and Jana Roithová*[a]

The Eschenmoser coupling reaction (ECR) of thioamides with electrophiles is believed to proceed via thiirane intermediates. However, little is known about converting the intermediates into ECR products. Previous mechanistic studies involved external thiophiles to remove the sulfur atom from the intermediates. In this work, an ECR proceeding without any thiophilic agent or base is studied by electrospray ionization-mass spectrometry. ESI-MS enables the detection of the so-far elusive polysulfide species S^n, with *n* ranging from 2 to 16 sulfur atoms, proposed to be the key species leading to product formation. Integrating observations from ion mobility spectrometry, ion spectroscopy, and reaction monitoring via flow chemistry coupled with mass spectrometry provides a comprehensive understanding of the reaction mechanism and uncovers the autocatalytic nature of the ECR reaction.

Introduction

The Eschenmoser coupling reaction (ECR)[1] of thioamides with electrophiles has been exploited in the past decades to synthesize numerous vinylogous amides and urethanes.[2–4] The mechanism involves the formation of an α-thioiminium salt (Scheme 1).[5,6] The transformation of the α-thioiminium into the product likely proceeds via a thiirane intermediate, as indirect evidence suggests.[7–9] The rate and yield of the ECR increase in the presence of thiophilic P(III) compounds,[2–4] which abstract the sulfur atom from the thiirane intermediates, leading to the formation of product alkenes and thiophosphates or phosphine-sulfides.[10–12] The ECR between 3-bromooxindole (**1**) and thiobenzamide (**2**) proceeds efficiently even without any thiophilic agent or base.[13,14] The sulfur atom is probably removed from the reaction intermediates by an *in-situ* formed thiophile because a spontaneous extrusion is improbable.

The rate of sulfur extrusion from isolated thiiranes depends on the thiirane concentration and does not strictly follow the first-order kinetics, implying that the abstraction of the sulfur atom is carried out by another thiirane or by another sulfur atom acceptor.[15–20] Previous studies showed that the sulfur extrusion rate increases with solvent polarity, suggesting the involvement of a polar or ionic transition state.[21] Moreover, adding acetic acid reduces the reaction rate, which supports the participation of thiolates.[21] In contrast, adding radical scavengers does not influence the reaction, thus excluding alternative radical pathway mechanisms. Finally, reactants with anionic sulfur functions, such as thiolates (e.g., thiophenoxide), catalyze the sulfur extraction from thiiranes.[22] Based on this information, a mechanism involving the growth of a sulfur chain on the intermediates was proposed until the stable cyclo-S_8 allotrope could be cleaved off.[17,18,21]

In this work, the intermediates in the ECR between **1** and **2** (Scheme 1) were monitored and characterized using electrospray ionization mass spectrometry (ESI-MS). The sensitivity of mass spectrometry enables the detection of low-concentration species, making it a tool of choice to detect and investigate reactive intermediates.[23–27] Along with online reaction monitoring, mass spectrometry offers a variety of add-on methods to gain mechanistic insights.[6,28–31] We coupled mass detection with ion mobility spectrometry to detect the presence of isomers[32–34] and used ion spectroscopy to characterize the structure of the reaction intermediates.[35,36] Details about reaction kinetics in solution were gathered using delayed reactant labeling,[31,37,38] and flow chemistry.[39] Combining all results from the individual methods provides a comprehensive view of the reaction mechanism and reveals the autocatalytic behavior of the ECR reaction.

Results and Discussion

Detection of the intermediates in the Eschenmoser coupling reaction by Electrospray Ionization Mass Spectrometry (ESI-MS). The ESI-MS monitoring of the reaction between **1** and **2** (1:5 ratio in DMF) shows a rapid formation of the reaction intermediates (*m/z* 269.07 - Figure 1a, see Scheme 1 for the possible structures) along with a depletion of $[\mathbf{1}\text{-Br}]^+$ (*m/z* 132.04 – formed by the loss of bromide from **1** during the ionization). Due to its poor ionization efficiency, thiobenzamide (**2**) is not detected in the ESI(+) experiments. The detected intermediates can correspond either to the α-thioiminium or protonated thiirane species. Therefore, the presence of these

[a] Dr. Q. Duez,[+] Prof. Dr. J. Roithová
Institute for Molecules and Materials, Faculty of Science, Radboud University, Heyendaalseweg 135, 6525 AJ Nijmegen, The Netherlands
E-mail: q.duez@science.ru.nl
j.roithova@science.ru.nl
[b] L. Marek,[+] Dr. J. Váňa, Prof. Dr. J. Hanusek
Institute of Organic Chemistry and Technology, Faculty of Chemical Technology, University of Pardubice, Studentská 573, CZ532 10 Pardubice, The Czech Republic
E-mail: Hanusek@upce.cz
[+] Contributed equally to this study

Supporting information for this article is available on the WWW under https://doi.org/10.1002/chem.202303619

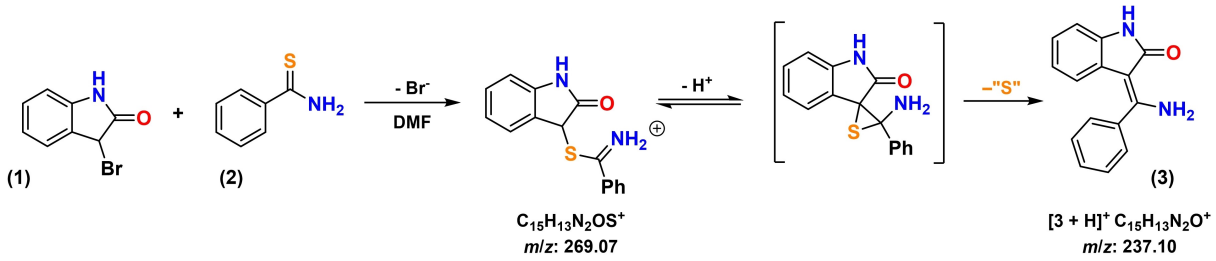

Scheme 1. The conventional mechanism for the Eschenmoser reaction investigated in this report.

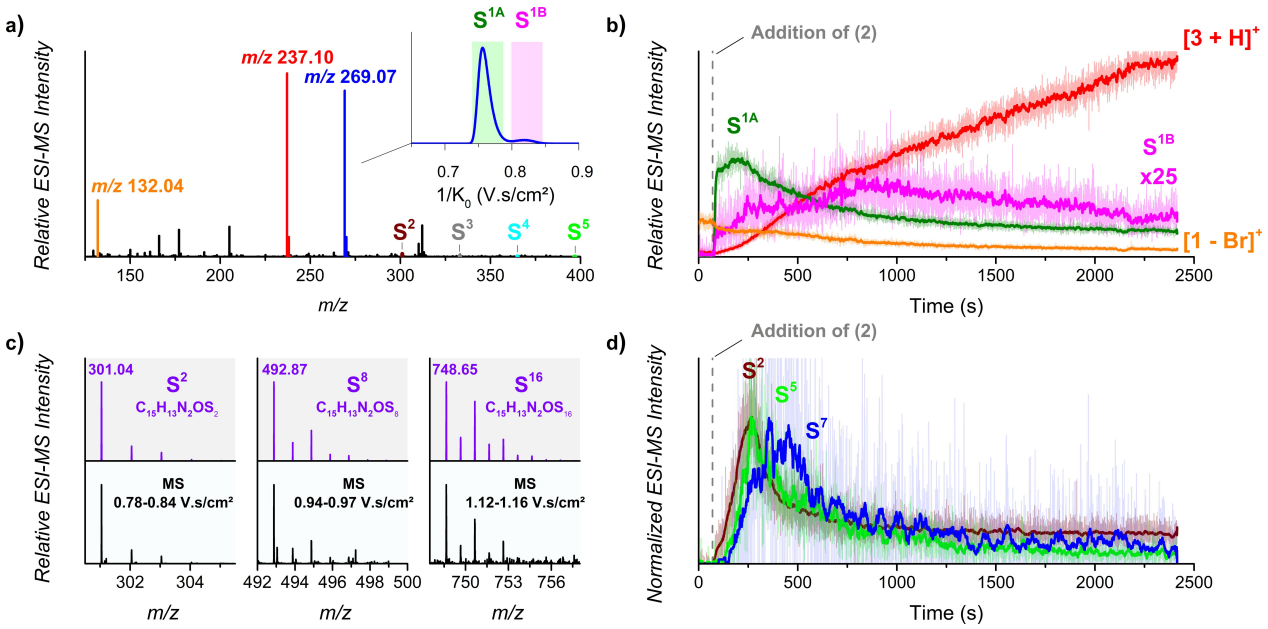

Figure 1. a) ESI-MS detection of the intermediate S^1 (m/z 269.07), the reactant $[1 - Br]^+$ (*m/z* 132.04), and protonated product $[3+H]^+$ (*m/z* 237.10) upon mixing 5 mM of **1** with 5 eq. of **2** in DMF. Inset: Ion mobility separation of two isomeric structures for S^1. S^{1A} denotes the ions detected at inverse mobilities 0.74-0.78 V.s/cm^2, and S^{1B} the ions detected at inverse mobilities 0.8-0.84 V.s/cm^2. **b)** Time evolution of the intensities of the individual isomers S^{1A} and S^{1B} and the product **3**. The relative intensity of S^{1B} was multiplied by 25. **c)** Detection of polysulfide S^n intermediates in the reaction mixture. Top: Simulated isotopic pattern for S^2, S^8 and S^{16}. Bottom: Experimental mass spectra filtered for selected inverse mobility ranges. **d)** Time evolution of S^2 (wine), S^5 (green), and S^7 (blue). The transparent lines are experimental ion chromatograms, and the bold lines are smoothed curves by point averaging. For better visualization, the smoothed curves are normalized.

isomeric species was evaluated by ion mobility spectrometry (IMS), which separates ions in the gas phase based on their size and shape.[40–42] The mobilogram of the *m/z* 269.07 ions reveals the presence of two isomers with distinct inverse mobilities (1/K_0): S^{1A} and S^{1B} (Figure 1a). The time evolution of the signals shows that S^{1A} forms nearly immediately, while S^{1B} appears with a slower kinetics (Figure 1b). The ECR product **3** (detected as $[3+H]^+$ at *m/z* 237.10) appears after a time lag. In comparison, NMR analysis of the reaction mixture after 2 min of reaction does not indicate any signals corresponding to the suggested intermediates (Figure S1).

Polysulfide species, having the same elemental composition as the S^1 intermediates but more sulfur atoms (S^n, with *n* being the number of sulfur atoms), were also detected. Based on their accurate masses and isotopic patterns, S^n intermediates with up to 16 sulfur atoms could be identified (Figure 1c and Table S1). The time profiles indicate that the polysulfide ions are formed with a slower kinetics than the initially formed S^{1A} intermediate. S^{2-4} are formed after a similar time, and larger polysulfides are produced later (see Figure S2). The time evolutions can only be followed up to S^7 because of the low abundance of larger polysulfide intermediates.

When the reaction is carried out at the molar concentrations, a precipitate is formed. The analysis of the precipitate by atmospheric-pressure chemical-ionization mass spectrometry with a solid probe (APCI-MS – details in SI) showed some of the polysulfide intermediates and elemental sulfur with up to 11 sulfur atoms (Figure S3).

Structural characterization of the intermediates. The classical analysis of the structure of mass-selected ions by collision-induced dissociation (CID) experiments did not help to assign or distinguish the structures of the detected S^{1A} and S^{1B} intermediates. Indeed, the mass- and ion-mobility-selected S^{1A} and S^{1B} have almost identical fragmentation patterns, showing the neutral loss of thiobenzamide, HS$^\bullet$, and NH_3 with similar intensities (Figure S4). Most likely, the interconversion of the

isomers requires less energy than the fragmentation, making the CID pattern of both isomers hard to distinguish. Alternatively, the ions have similar structures, leading to the analogous fragmentation pattern.

The structure of mass-selected ions is best assigned using ion spectroscopy.[35,36] For the spectroscopic characterization by cryogenic infrared photodissociation (IRPD), the reaction was carried out using a flow reactor with a constant reaction time (Figure S17). Moreover, acetonitrile was used as a solvent to improve the signal stability. Under these conditions, only $\mathbf{S}^{1A}$ could be detected (Figure S5 for the ion mobility-mass spectrometry analysis of the reaction mixture in acetonitrile). The IRPD spectrum of $\mathbf{S}^{1A}$ can be assigned based on a comparison with DFT calculations (Figure 2a). The experimental spectrum best agrees with the theoretical spectrum computed for the α-thioiminium isomer ($\mathbf{S}^{IR\text{-}A}$ in Figure 2b), which is also the most stable isomer. The alternative isomers lie higher in energy than $\mathbf{S}^{IR\text{-}A}$ and their theoretical IR spectra do not agree, or agree less well, with the experimental one. These isomers include the thiirane intermediate ($\mathbf{S}^{IR\text{-}B}$), an iminium ion resulting from the ring opening of thiirane ($\mathbf{S}^{IR\text{-}C}$), a protomer of the thiirane intermediate ($\mathbf{S}^{IR\text{-}D}$), or a tautomer of the α-thioiminium species ($\mathbf{S}^{IR\text{-}E}$). More candidate structures are presented in Figure S6.

The IRPD spectrum reveals two sharp bands at 3419 cm^{-1} and 3470 cm^{-1} that match well with the N–H stretching vibrations of the indole core (N_{ind}–H) and iminium group of $\mathbf{S}^{IR\text{-}A}$ (Figure 2b). One of the N–H bonds engages in hydrogen bonding with the carbonyl oxygen atom and appears as a broad band at about 2800 cm^{-1}, overlapping with the C–H vibration modes. The bands observed at 1710 and 1724 cm^{-1} are characteristic of a carbonyl stretching mode involved in Fermi resonance. The observation of two IR bands near the expected carbonyl stretching frequencies has been reported for various indoles and oxindoles. It is attributed to the Fermi resonance between the carbonyl stretching mode and either an overtone or a combination of other vibrational modes.[43–45] In this case, the carbonyl stretching is likely coupled to an overtone transition of a mode involving N–H rocking and ring breathing (Figure S7). For comparison, the IRPD spectrum recorded for the Eschenmoser product $[\mathbf{3}+H]^+$ shown in Figure 3 does not show any band above 1700 cm^{-1} because of the protonation of the carbonyl moiety.

The predicted IR spectrum of $\mathbf{S}^{IR\text{-}C}$ in Figure 2d could also be considered a good match with the experimental spectrum. However, the spectral separation of the carbonyl stretching band (ν(C=O)) and the N–H deformation band (δ(N–H)) for the

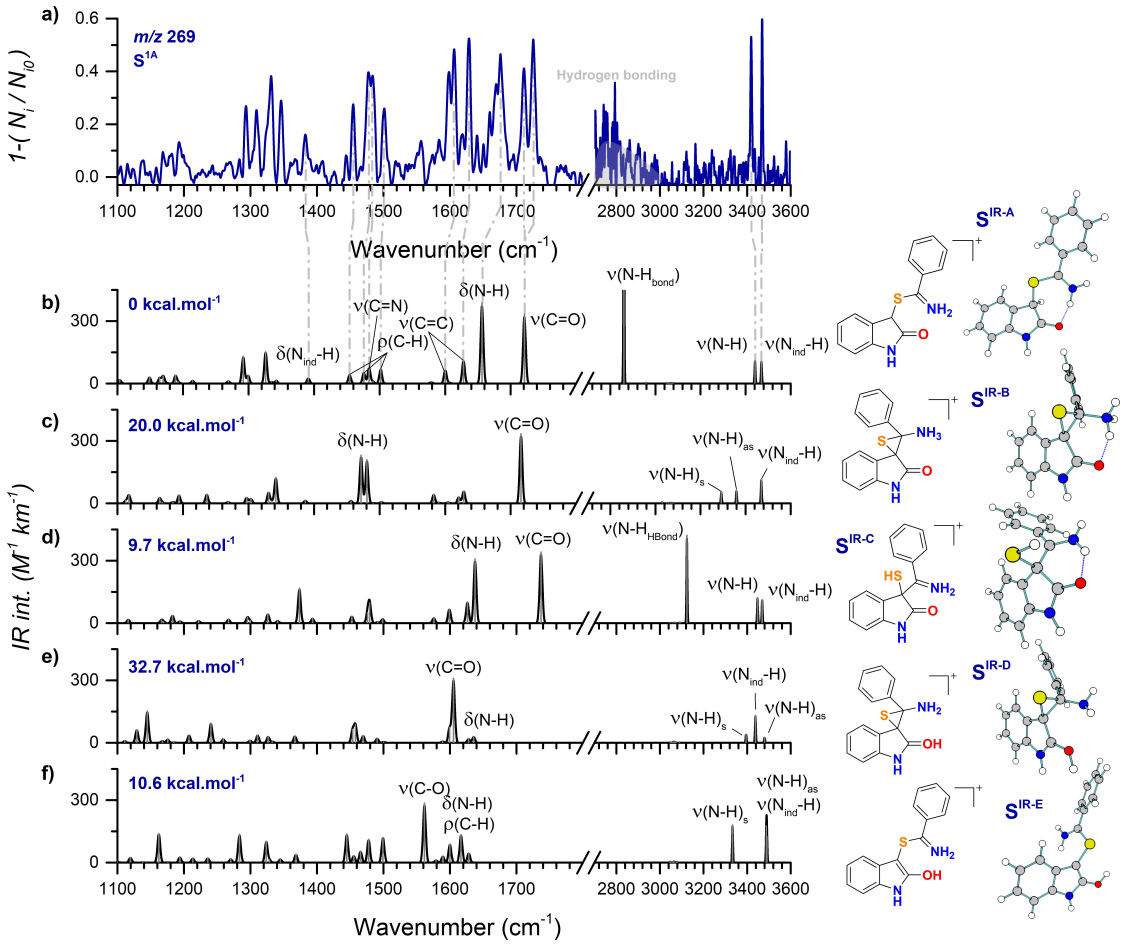

Figure 2. a) IR photodissociation spectrum of $\mathbf{S}^{1A}$ measured by helium tagging photodissociation spectroscopy. **b–f)** Theoretical IR spectra for five possible structures of $\mathbf{S}^{1A}$ (B3LYP-GD3BJ/6-311+G(2d,p)). The grey dashed lines correspond to the most probable assignment of the experimental bands. The indicated relative energies correspond to free energies.

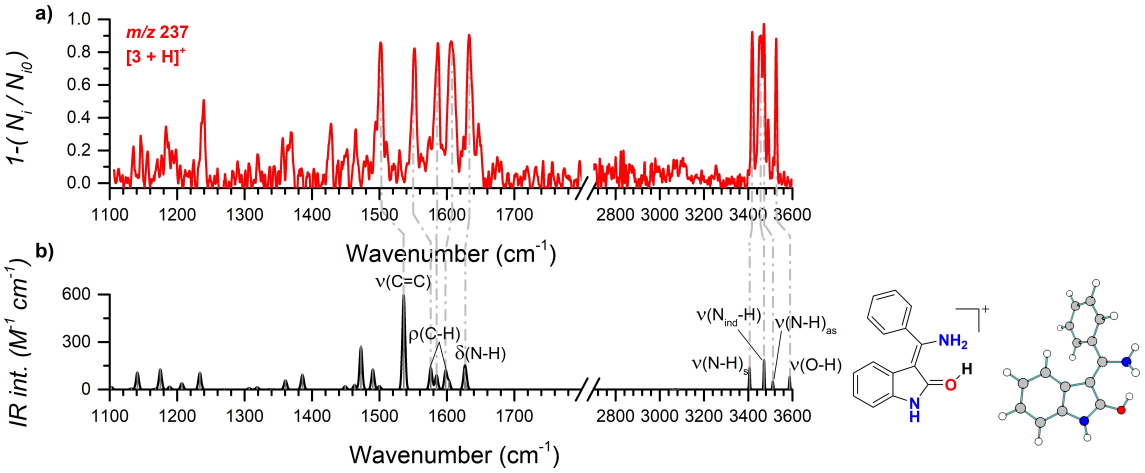

Figure 3. a) IR photodissociation spectrum of $[3+H]^+$ measured by helium tagging photodissociation spectroscopy. **b)** Theoretical IR spectrum for $[3+H]^+$ (B3LYP-GD3BJ/6-311+G(2d,p)). The grey dashed lines correspond to the most probable assignment of the experimental bands.

ring-opened thiirane is much larger than that for α-thioiminium $\mathbf{S}^{IR\text{-}A}$. The latter agreed better with the experiments.

The structure of the second isomer $\mathbf{S}^{1B}$ cannot be directly obtained from the IRPD or CID data. The kinetic profile of $\mathbf{S}^{1B}$ suggests that it is formed from $\mathbf{S}^{1A}$ (assigned to $\mathbf{S}^{IR\text{-}A}$, the α-thioiminium species). Hence, $\mathbf{S}^{1B}$ does not correspond to a different protomer ($\mathbf{S}^{IR\text{-}E}$ in Figure 2f). The most obvious suggestion would be that the ions correspond to the thiirane intermediate ($\mathbf{S}^{IR\text{-}B}$), which is most likely neutral in solution. The thiirane intermediate can be protonated at the amino group ($\mathbf{S}^{IR\text{-}B}$) or the sulfur atom. According to our DFT calculations, the sulfur protonation does not lead to a stable isomer but initiates the thiirane's ring-opening ($\mathbf{S}^{IR\text{-}C}$). The $\mathbf{S}^{IR\text{-}C}$ isomer lies lower in energy than $\mathbf{S}^{IR\text{-}B}$, which suggests that the $\mathbf{S}^{1B}$ ions correspond to the ring-opened thiiranes $\mathbf{S}^{IR\text{-}C}$. This assignment is consistent with the identical CID patterns of $\mathbf{S}^{1A}$ and $\mathbf{S}^{1B}$ (Figure S4), suggesting that they are structurally similar or connected via small energy barriers. $\mathbf{S}^{IR\text{-}C}$ can easily isomerize into $\mathbf{S}^{IR\text{-}E}$, a tautomer of the α-thioiminium $\mathbf{S}^{IR\text{-}A}$ (Figure S8), having similar dissociation patterns. The isomer $\mathbf{S}^{1B}$ is thus assigned to the ring-opened thiirane $\mathbf{S}^{IR\text{-}C}$. These ions are most likely formed during the ionization and, therefore, report on the neutral thiirane intermediates in solution. This interpretation is consistent with the low ionization efficiency and problems detecting these ions from the solution.

The structural characterization of the polysulfide intermediates cannot take advantage of ion spectroscopy because of their low ion abundance. The CID spectra of $\mathbf{S}^2$ and $\mathbf{S}^4$ are shown in Figure 4. Like for $\mathbf{S}^{1B}$ ions, the intermediates are probably protonated during ESI, yielding open structures similar to $\mathbf{S}^{IR\text{-}C}$. The collisional activation then leads to the nucleophilic attack of the iminium ion by one of the sulfur atoms. The exclusive attack of the terminal sulfur atom is observed for $\mathbf{S}^2$, leading to the breaking of the S–S bond and forming protonated thiobenzamide and 3-thioxo-2-oxindole (Figure 4a). The intermediates with more sulfur atoms fragment analogously (Figure S9). All sulfur atoms, but the one bound to the indole, can initiate the fragmentation. In addition, the formation of radical cations is observed (fragments with odd *m/z*). These fragments can be explained by the thiirane rearrangement into a macrocyclic polysulfide structure, which opens by the protonation at the carbon atom of the indole moiety (Figure 4b). The C–S or S–S bonds can undergo homolytic cleavages, explaining the odd-mass fragments in the CID spectra of the polysulfide intermediates.

Reaction kinetics in solution reveals an autocatalytic behavior. The kinetics of the ECR exhibits a strong dependence on the concentration of reactants. The ECR reaction with 5 mM of **1** and 2 eq. of **2** showed a longer lag time before the growth of the product ions compared to the experiment with 5 eq. of **2** (Figure S10a and Figure 1). Additionally, the production and depletion of the polysulfide species occurred at a slower rate (Figures S10b and S11). For example, the maximum abundance of $\mathbf{S}^2$ was detected after 7.5 minutes in the reaction with 2 equivalents of **2**, whereas it was observed after only 3 minutes when 5 equivalents of **2** were added. NMR studies corroborate the ESI-MS observations, demonstrating a clear association between the ECR product formation kinetics and the reactant concentration (Figures S1 and S12).

To better understand how the ECR kinetics depends on the reactant concentration and how the $\mathbf{S}^{1A}/\mathbf{S}^{1B}$ and polysulfide intermediates are related to the formation of the product, flow chemistry experiments were carried out. These experiments were designed to monitor the evolution of the ECR after a selected reaction time while continuously increasing the reactant concentration (Figure 5). They enable the rapid screening of the effects of the reaction conditions. The experiments could be used, for instance, to establish the optimal reaction conditions for forming a given product with a limited reaction time. As shown in Figure 5a, the flow setup comprises five syringe pumps. The flow rates of the syringe pumps containing 3-bromoxindole (**1**) and thiobenzamide (**2**) were programmed to increase continuously from 0 to 20 $\mu L\,min^{-1}$, with the same gradient to maintain the 1:1 ratio between the two reactants. The increase in the flow rate was counterbalanced by the rates of two additional syringe pumps filled with DMF, keeping the

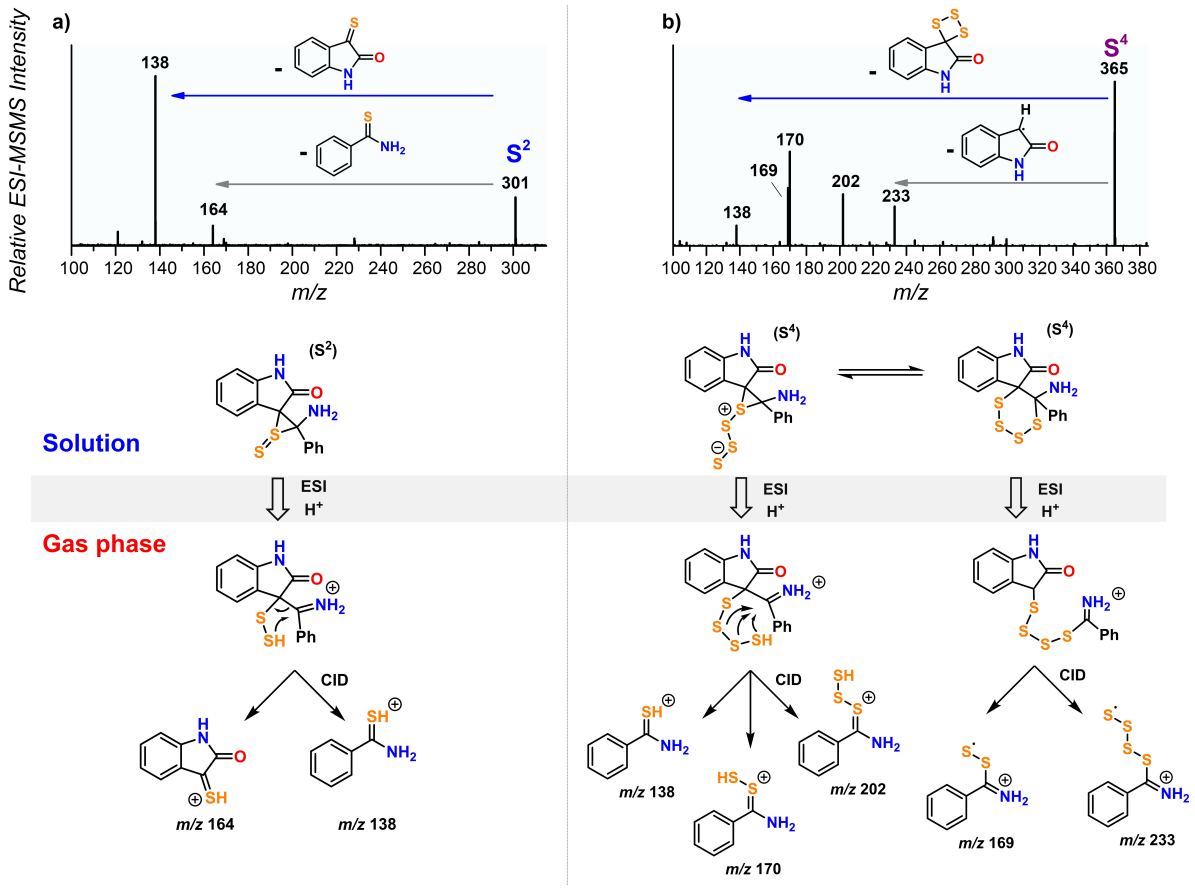

Figure 4. Collision-induced dissociation of mass- and mobility-selected **a)** S^2 and **b)** S^4 after 4 minutes of reaction time. The scheme shows probable fragmentation pathways and fragment structures; the fragmentations can also include the proton transfer from one fragment to another.

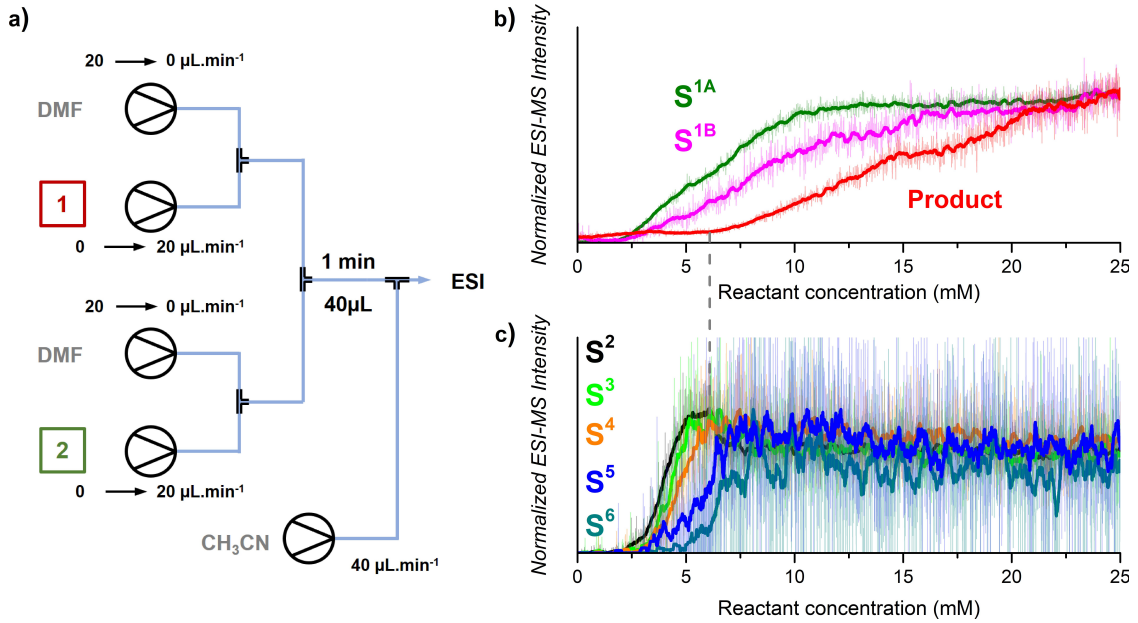

Figure 5. ESI-MS monitoring the ECR after a fixed reaction time while increasing reactant concentration using a flow reactor. **a)** Schematic representation of the flow setup. **b)** Normalized time evolution of S^{1A} (olive), S^{1B} (magenta), and ECR product (red). **c)** Time evolution of S^2 (black), S^3 (green), S^4 (orange), S^5 (blue) and S^6 (dark cyan). The transparent lines are the experimental ion chromatograms, and the bold lines are the curves smoothed by point averaging. For a better visualization, the smoothed curves are normalized.

overall flow constant. The reaction mixture was allowed to react for one minute, then diluted with acetonitrile and directly guided into the mass spectrometer.

With the increasing reactant concentrations, $\mathbf{S^{1A}}$ and $\mathbf{S^{1B}}$ are the first species to be generated within one minute of the reaction time. The polysulfide species appear sequentially, with the longer chains being produced at a higher reactant concentration (Figure 5c and Figure S13). This suggests that the growth mechanism of polysulfide species involves the consecutive addition of sulfur atoms. Interestingly, the ECR product only grows significantly when polysulfide species are present, thus indicating that $\mathbf{S}^n$ intermediates are the key species driving the product formation.

Delayed reactant labeling (DRL) experiments provide a quantitative connection between the solution kinetics and ESI-MS.[37,38] The reaction mixture is spiked with an isotopically labeled reagent after a time delay, leading to the generation of the labeled reaction intermediates. Since the isotopically labeled and unlabeled ions share the same ionization efficiency, their relative abundance in the mass spectrum directly reports on the relative concentration of their precursors in solution, enabling the determination of quantitative kinetic data. The rate at which the concentrations of labeled and unlabeled species equilibrate provides insights into the reaction rates of the corresponding intermediates in solution.[37] For the present reaction, 1 eq. of thiobenzamide (**2**) and 1 eq. of D_5-labeled thiobenzamide ($\mathbf{2^{D5}}$) were sequentially added with various delays to a solution of **1** in DMF. After adding D_5-labeled thiobenzamide, the labeled reaction intermediates $\mathbf{S^{1A\text{-}D5}}$, $\mathbf{S^{1B\text{-}D5}}$, $\mathbf{S^{2\text{-}D5}}$, and the ECR product $\mathbf{3^{D5}}$ are generated (Figure 6a). Other polysulfide species $\mathbf{S^{n\text{-}D5}}$ are also observed, but their reaction kinetics cannot be followed because of their low abundance. The delay was varied to show whether the reaction progress and formation of the polysulfide species at longer reaction times affect the kinetics of the key intermediates.

Regardless of the time delay, the kinetics with which the precursors of $\mathbf{S^{1A}}$ and $\mathbf{S^{1B}}$ react in solution are strikingly different (Figure 6b). The relative concentrations of $\mathbf{S^{1A}}$ and $\mathbf{S^{1A–D5}}$ almost immediately reach the equilibrium, which indicates a short half-life of $\mathbf{S^{1A}}$ (MS-observed rate $k_{MS} > 0.5\ s^{-1}$, see Equations S1 and S2 and ref.[38]). Hence, $\mathbf{S^{1A}}$ is either in a fast equilibrium with the reactants or reacts rapidly towards the following reaction intermediates. On the other hand, the equilibration of $\mathbf{S^{1B}}$ and $\mathbf{S^{1B–D5}}$ is much slower, suggesting that the thiirane is a long-lived intermediate in solution and its transformation is the rate-determining step of the reaction (Table S2).[46] Although the thiirane accumulates in solution, the ESI-MS signal of $\mathbf{S^{1B}}$ is low, which is expected for the neutral thiirane intermediates, as discussed above. The thiirane needs to be protonated for detection, decreasing its ionization efficiency compared to the α-thioiminium intermediate $\mathbf{S^{1A}}$ (Figure 1). The $\mathbf{S^2}$ intermediates equilibrate much faster. The fast equilibrium of $\mathbf{S^2}$ with the reactants is improbable; therefore, these intermediates likely react quickly towards other intermediates along the reaction path or towards the products.

Interestingly, the half-life of the thiirane (detected as $\mathbf{S^{1B}}$) decreases with increasing delays between the addition of **2** and $\mathbf{2^{D5}}$ (Table S2). This trend is also noticeable for $\mathbf{S^2}$. At longer reaction times, the transformation of the primary thiirane intermediates towards the secondary intermediates and products becomes faster (*i.e.*, their half-life is shorter), which coincides with the formation of the polysulfide species $\mathbf{S}^n$ (Figure 1 and S1).

The initial slow phase of the ECR can be overcome by increasing the concentration of the reactants. Doubling the concentrations of the reactants (10 mM **1, 2**, and $\mathbf{2^{D5}}$) leads to a fast reaction, where no time-lags are observed, and all intermediates are in apparent equilibrium with the reactants (Figure S14). This suggests that the transformation of the thiirane does not represent a reaction bottleneck under these conditions. This finding is consistent with the key role of polysulfide species in the transformation of the thiirane. The flow experiments showed that the formation of the polysulfide species is much slower at 5 mM concentration than at 10 mM concentration (see Figure 5c). Though the results were obtained under the flow conditions and 1 min reaction time, they capture the effect of the concentration on the rate of the polysulfide formation and explain well the striking difference of the reaction kinetics determined by the DRL at different concentrations.

Hence, the results suggest that the thiobenzamide (**2**) and 3-bromoxindole (**1**) generate an α-thioiminium species $\mathbf{S^{1A}}$, which interconverts in the thiirane, detected as protonated $\mathbf{S^{1B}}$. Next, the polysulfide species, detected as protonated $\mathbf{S}^n$, react as thiophiles with the thiirane, generating a molecule of product and ($\mathbf{S}^{n+1}$ – **H**). The remaining question is about the initial formation of the $\mathbf{S^2}$ species. The data imply that ($\mathbf{S^2}$ – **H**) must be generated from a slow bimolecular reaction involving two thiiranes, as suggested in the literature.[16,17,19,20] Once ($\mathbf{S^2}$ – **H**) is formed, the follow-up reaction with another thiirane, generating ($\mathbf{S^3}$ – **H**) and the product molecule, is fast. A complete description of the proposed mechanism is shown in Scheme 2.

Conclusions

In this work, the Eschenmoser coupling reaction between 3-bromooxindole (**1**) and thiobenzamide (**2**) (ECR, Scheme 1), which proceeds without any base or external thiophilic agent to assist the sulfur removal, was studied by different mass spectrometry techniques.[12,13,37] The key reaction intermediates were trapped and characterized, and the investigation of the reaction kinetics in solution uncovered the origin of the autocatalytic nature of this reaction.

The ECR begins with the rapid formation of two isomeric intermediates, detected as $\mathbf{S^{1A}}$ and $\mathbf{S^{1B}}$, exhibiting different formation and depletion kinetics. $\mathbf{S^{1A}}$ was spectroscopically characterized as an α-thioiminium species, and $\mathbf{S^{1B}}$ was attributed to the protonated thiirane intermediate. Furthermore, elusive polysulfide species $\mathbf{S}^n$ were detected, with *n* ranging from 2 to 16 sulfur atoms. Flow chemistry experiments unveiled that the lag phase in the appearance of the ECR product is correlated with the sequential generation of the

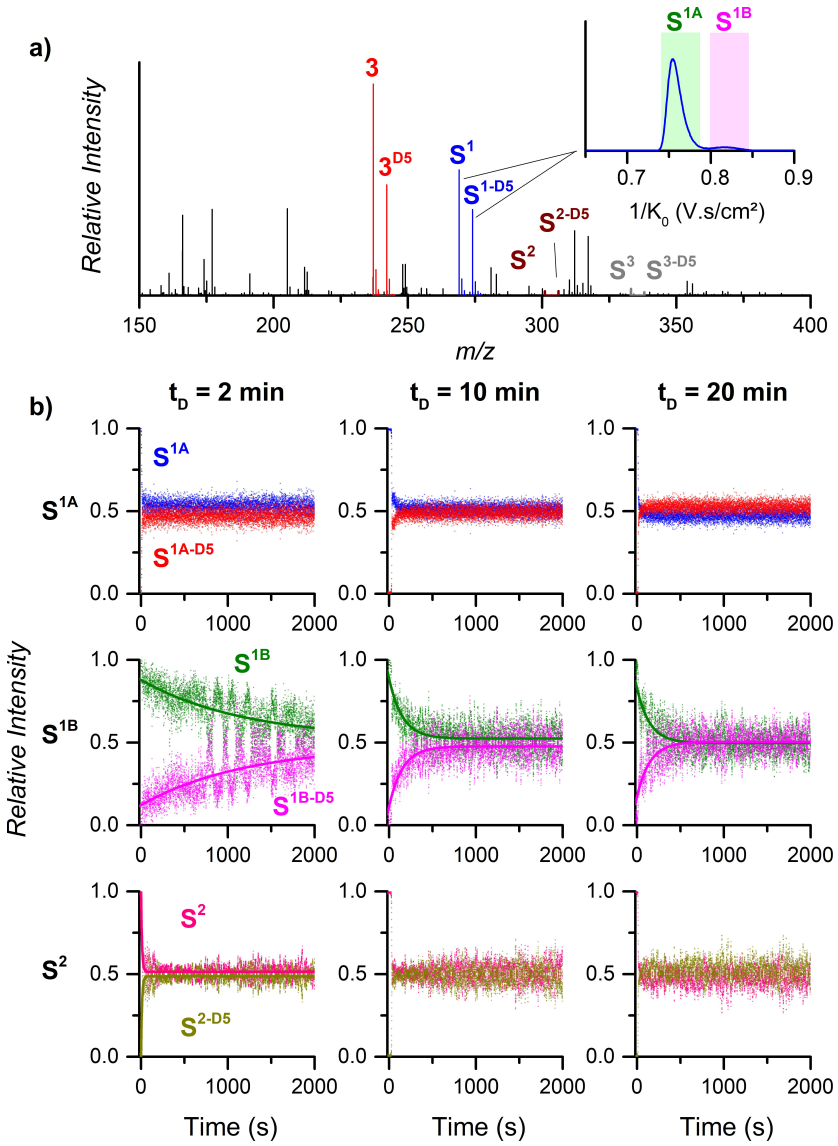

Figure 6. a) ESI-MS detection of unlabeled and D5-labeled Eschenmoser intermediate $S^1/S^{1\text{-}D5}$ (*m/z* 269.07–274.10) and products $3/3^{D5}$ (*m/z* 237.10–242.13) upon mixing 5 mM of **1** with 1 eq. of **2** and 1 eq. of 2^{D5} in DMF; 2^{D5} was added with different time delays (indicated in the figure). $S^2/S^{2\text{-}D5}$ and $S^3/S^{3\text{-}D5}$ ions are also highlighted. Inset: Ion mobility separation of S^{1A} and S^{1B}. **b)** Time evolution of the relative intensities of mass- and mobility-selected (top) S^{1A} and $S^{1A\text{-}D5}$, (middle) S^{1B} and $S^{1B\text{-}D5}$, and (bottom) S^2 and $S^{2\text{-}D5}$ after adding D_5-thiobenzamide in the delayed reactant labeling experiment. The dots are the experimental data points; the lines correspond to the fits of the experimental data by the first-order kinetic functions (Equations S1 and S2). The data of the experiments for which the equilibration of labeled and unlabeled species was nearly immediate were not fitted.

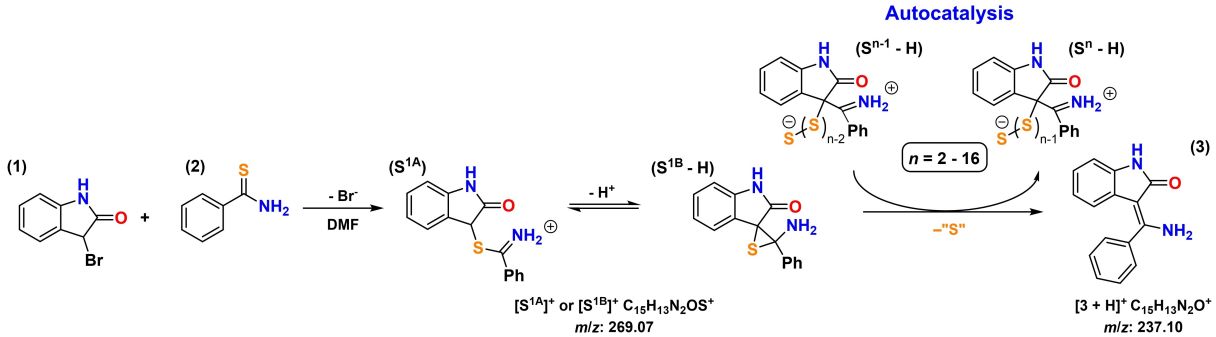

Scheme 2. Proposed mechanism for the ECR based on the ESI-MS results gathered in this work.

polysulfide species. At small reactant concentrations, the formation of the polysulfide species is slow, resulting in a larger lag before the product formation. The lag disappears with the larger reactant concentrations. Furthermore, delayed reactant labeling experiments showed that the kinetics with which the thiirane and the thiirane-S-sulfide react in solution accelerated with the increasing concentration of polysulfides species, thus indicating that a sulfur abstraction between polysulfides and the thiirane is the key reaction driving the product formation.

As a summary, the reactants **1** and **2** generate an α-thioiminium salt $\mathbf{S^{1A}}$. The α-thiominium salt then interconverts in the thiirane intermediate (detected as protonated $\mathbf{S^{1B}}$), which reacts further with another thiirane to produce ($\mathbf{S^2}$ – **H**) and a molecule of product **3**. This reaction step is slow and represents the rate-determining step. However, with the increasing reaction time, the polysulfide intermediates, detected as $\mathbf{S^n}$, increase in concentration and react fast with the thiirane to form the product **3** and larger polysulfides, detected as $\mathbf{S^{n+1}}$. The reaction with the polysulfide intermediates circumvents the slow reaction step between two molecules of thiirane (Scheme 2). Hence, the ECR is autocatalytic, with polysulfide species acting as internal thiophiles and being the key species leading to product formation.

Experimental section

Materials. Thiobenzamide is commercially available (Sigma-Aldrich), and 3-bromoxindole was synthesized using a procedure described in the literature.[14] The synthesis and characterization of D_5-thiobenzamide is described in Supplementary Information.

Mass spectrometry. Ion mobility-mass spectrometry experiments were performed with a timsToF instrument (Bruker, Germany) equipped with an ESI source. Ions were electrosprayed in positive mode with a source voltage of + 5.5 kV, with a Nebulizer of 0.2 Bar, a drying gas flow of 2 L min^{-1}, and the End Plate Offset set to 500 V.

Typical ion transfer voltages were quadrupole ion energy = 3 eV and collision energy = 5 eV. The mass range scanned by the ToF analyzer was *m/z* 100–1000. TIMS experiments were performed in N_2 using the imeX Detect mode by scanning ion mobility from 0.3 V.s.cm^{-2} to 1.5 V.s.cm^{-2}. The accumulation time was set to 20 ms in order to minimize ion activation in the ion mobility region.

All the reaction mixtures were prepared in dry DMF (Sigma-Aldrich). Typically, a 2 mL solution of 3-bromoxindole (5 mM) is continuously stirred. After one minute, 80 μL of a 250 mM solution of thiobenzamide is added to the reaction mixture. Final concentrations: 4.81 mM of 3-bromoxindole and 9.61 mM of thiobenzamide (for 1:2 experiments). Flow chemistry experiments were carried out using Labm8 syringe pumps. Additional details regarding mass spectrometry, preparation of reaction mixtures, and infusion in the mass spectrometer can be found in Supplementary Information, along with details regarding delayed reactant labeling experiments.

Gas-phase infrared photodissociation (IRPD) experiments were performed with a custom-built instrument based on a TSQ-7000.[36] In this instrument; the mass-selected ions are guided through a quadrupole bender and an octupole to a linear wire quadrupole trap operating at 3 K. The ions are trapped and thermalized by pulses of helium gas. The thermalized ions form weakly bound adducts with helium. The trapped ions are irradiated in odd cycles. Finally, the ions are extracted from the trap, mass-analyzed by a quadrupole, and detected by a Daly-type detector. The photon absorption was monitored as the depletion of the number of helium adducts detected with ($N_i(\nu)$) or without ($N_{i0}(\nu)$) IR irradiation. The IR photons were generated by a tunable OPO/ OPA photon source. The flow setup used for IRPD experiments is shown in Figure S17.

Computational details. DFT calculations were carried out with B3LYP-GD3BJ/6-311 + G(2d,p)[47–49] as implemented in the Gaussian 16 package.[50] All reported structures correspond to potential energy surface minima, as confirmed by analyses of the corresponding Hessian matrixes. Reported energies include zero-point vibrational energy corrections and thermal corrections calculated at the same level of theory. The reported IR spectra were scaled by 0.98 for the range below 2500 cm^{-1} and 0.96 for the range above 2500 cm^{-1}.

Supporting Information

Additional details about materials and methods are presented in the Supporting Information, along with additional control experiments. The authors have cited the following references in Supporting Information.[51–53]

Acknowledgements

The authors are grateful for financial support from the Dutch Research Council NOW (VI.C.192.044 and OCENW.KLEIN.348).

Conflict of Interests

There are no conflicts of interest to declare.

Data Availability Statement

The data that support the findings of this study are openly available in Radboud Data Repository at https://doi.org/10.34973/fvh1-nf46. The cartesian coordinates of the computed structures are available as supplementary information.

Keywords: Mass spectrometry · Autocatalysis · Reaction mechanisms · Vibrational spectroscopy · Ion mobility · Flow chemistry · Density functional theory calculations

[1] A. Fischli, A. Eschenmoser, *Angew. Chem. Int. Ed.* **1967**, *6*, 866–868.
[2] K. Shiosaki, in *Comprehensive Organic Synthesis*, (Eds. B. Trost and I. Fleming), Elsevier, **1991**, pp. 865–892.
[3] S. Braverman, M. Cherkinsky, in *Comprehensive Organic Synthesis II*, (Ed. P. Knochel), Elsevier, **2014**, pp. 887–943.
[4] S. R. Hussaini, R. R. Chamala, Z. Wang, *Tetrahedron.* **2015**, *71*, 6017–6086.
[5] R. E. Ireland, F. R. Brown, *J. Org. Chem.* **1980**, *45*, 1868–1880.
[6] B. A. D. Neto, A. A. M. Lapis, A. B. Bernd, D. Russowsky, *Tetrahedron* **2009**, *65*, 2484–2496.
[7] E. B. Knott, *J. Chem. Soc.* **1955**, 916–927.
[8] B. Roth, R. Laube, M. Y. Tidwell, B. S. Rauckman, *J. Org. Chem.* **1980**, *45*, 3651–3657.

[9] N. D. Koduri, B. Hileman, J. D. Cox, H. Scott, P. Hoang, A. Robbins, K. Bowers, L. Tsebaot, K. Miao, M. Castaneda, M. Coffin, G. Wei, T. D. W. Claridge, K. P. Roberts, S. R. Hussaini, *RSC Adv.* **2013**, *3*, 181–188.
[10] R. E. Davis, *J. Org. Chem.* **1958**, *23*, 1767–1768.
[11] N. P. Neureiter, F. G. Bordwell, *J. Am. Chem. Soc.* **1959**, *81*, 578–580.
[12] D. B. Denney, M. J. Boskin, *J. Am. Chem. Soc.* **1960**, *82*, 4736–4738.
[13] R. Kammel, D. Tarabová, B. Brož, V. Hladíková, J. Hanusek, *Tetrahedron.* **2017**, *73*, 1861–1866.
[14] L. Marek, L. Kolman, J. Vana, J. Svoboda, J. Hanusek, *Beil. J. Org. Chem.* **2021**, *17*, 527–539.
[15] K. P. C. Vollhart, R. G. Bergman, *J. Am. Chem. Soc.* **1973**, *95*, 7538–7539.
[16] E. Lutz, J.-F. Biellmann, *Tetrahedron Lett.* **1985**, *26*, 2789–2792.
[17] W. Chew, D. N. Harpp, *Tetrahedron Lett.* **1992**, *33*, 45–48.
[18] W. Chew, R. C. Hynes, D. N. Harpp, *J. Org. Chem.* **1993**, *58*, 4398–4404.
[19] Y. Steudel, R. Steudel, M. W. Wong, *Chem. Eur. J.* **2002**, *8*, 217–228.
[20] E. M. Lown, H. S. Sandhu, H. E. Gunning, O. P. Strausz, *J. Am. Chem. Soc.* **1968**, *90*, 7164–7165.
[21] W. Chew, D. N. Harpp, *J. Org. Chem.* **1993**, *58*, 4405–4410.
[22] R. Huisgen, *Phosphorus, Sulfur, and Silicon and the Related Elements.* **1989**, *43*, 63–94.
[23] A. Revesz, D. Schroder, T. A. Rokob, M. Havlik, B. Dolensky, *Angew. Chem. Int. Ed.* **2011**, *50*, 2401–2404.
[24] L. P. E. Yunker, Z. Ahmadi, J. R. Logan, W. Wu, T. Li, A. Martindale, A. G. Oliver, J. S. McIndoe, *Organometallics.* **2018**, *37*, 4297–4308.
[25] C. M. Choi, A. Kulesza, S. Daly, L. MacAleese, R. Antoine, P. Dugourd, F. Chirot, *Rapid Commun. Mass Spectrom.* **2019**, *33*, 28–34.
[26] R. G. Belli, Y. Wu, H. Ji, A. Joshi, L. P. E. Yunker, J. S. McIndoe, L. Rosenberg, *Inorg. Chem.* **2019**, *58*, 747–755.
[27] L. Polewski, A. Springer, K. Pagel, C. A. Schalley, *Acc. Chem. Res.* **2021**, *54*, 2445–2456.
[28] W. Jiang, A. Schäfer, P. C. Mohr, C. A. Schalley, *J. Am. Chem. Soc.* **2010**, *132*, 2309–2320.
[29] K. L. Vikse, J. S. McIndoe, *Pure Appl. Chem.* **2015**, *87*, 361–377.
[30] D. Van Craen, W. H. Rath, M. Huth, L. Kemp, C. Rauber, J. M. Wollschlager, C. A. Schalley, A. Valkonen, K. Rissanen, M. Albrecht, *J. Am. Chem. Soc.* **2017**, *139*, 16959–16966.
[31] J. Mehara, J. Roithová, *Chem. Sci.* **2020**, *11*, 11960–11972.
[32] M. M. Gaye, G. Nagy, D. E. Clemmer, N. L. Pohl, *Anal. Chem.* **2016**, *88*, 2335–2344.
[33] S. Poyer, C. Lopin-Bon, J. C. Jacquinet, J. Y. Salpin, R. Daniel, *Rapid. Commun. Mass Spectrom.* **2017**, *31*, 2003–2010.
[34] A. Galanti, J. Santoro, R. Mannancherry, Q. Duez, V. Diez-Cabanes, M. Valasek, J. De Winter, J. Cornil, P. Gerbaux, M. Mayor, P. Samori, *J. Am. Chem. Soc.* **2019**, *141*, 9273–9283.
[35] J. Jašík, J. Žabka, J. Roithová, D. Gerlich, *Int. J. Mass spectrom.* **2013**, *354–355*, 204–210.
[36] J. Roithová, A. Gray, E. Andris, J. Jašík, D. Gerlich, *Acc. Chem. Res.* **2016**, *49*, 223–230.
[37] L. Jasíková, M. Anania, S. Hybelbauerová, J. Roithová, *J. Am. Chem. Soc.* **2015**, *137*, 13647–13657.
[38] Q. Duez, P. Tinnemans, J. A. A. W. Elemans, J. Roithová, *Chem. Sci.* **2023**, *14*, 9759–9769.
[39] G. L. Tripodi, M. T. G. M. Derks, F. P. J. T. Rutjes, J. Roithová, *Chem.-Meth.* **2021**, *1*, 430–437.
[40] F. Lanucara, S. W. Holman, C. J. Gray, C. E. Eyers, *Nat. Chem.* **2014**, *6*, 281–294.
[41] V. Gabelica, E. Marklund, *Curr. Opin. Chem. Biol.* **2018**, *42*, 51–59.
[42] V. Gabelica, A. A. Shvartsburg, C. Afonso, P. Barran, J. L. P. Benesch, C. Bleiholder, M. T. Bowers, A. Bilbao, M. F. Bush, J. L. Campbell, I. D. G. Campuzano, T. Causon, B. H. Clowers, C. S. Creaser, E. De Pauw, J. Far, F. Fernandez-Lima, J. C. Fjeldsted, K. Giles, M. Groessl, C. J. Hogan, Jr., S. Hann, H. I. Kim, R. T. Kurulugama, J. C. May, J. A. McLean, K. Pagel, K. Richardson, M. E. Ridgeway, F. Rosu, F. Sobott, K. Thalassinos, S. J. Valentine, T. Wyttenbach, *Mass Spectrom. Rev.* **2019**, *38*, 291–320.
[43] A. E. Kellie, D. G. O'Sullivan, P. W. Sadler, *J. Chem. Soc.* **1956**, 3792–3796.
[44] A. H. Beckett, R. W. Daisley, J. Walker, *Tetrahedron.* **1968**, *24*, 6093–6109.
[45] J. M. Rodgers, R. M. Abaskharon, B. Ding, J. Chen, W. Zhang, F. Gai, *Phys. Chem. Chem. Phys.* **2017**, *19*, 16144–16150.
[46] L. Marek, J. Vana, J. Svoboda, J. Hanusek, *Beil. J. Org. Chem.* **2023**, *19*, 808–819.
[47] A. D. Becke, *J. Chem. Phys.* **1993**, *98*, 1372–1377.
[48] A. D. McLean, G. S. Chandler, *J. Chem. Phys.* **1980**, *72*, 5639–5648.
[49] S. Grimme, S. Ehrlich, L. Goerigk, *J. Comput. Chem.* **2011**, *32*, 1456–1465.
[50] e. a. M. J. Frisch, Gaussian 16, *Gaussian 16*, **2016**.
[51] G. T. Thomas, S. Donnecke, I. C. Chagunda, J. S. McIndoe, *Chem.-Meth.* **2022**, *2(1)*, e202100068.
[52] G. L. Tripodi, M. M. J. Dekker, J. Roithová, L. Que, Jr., *Angew. Chem. Int. Ed.* **2021**, *60*, 7126–7131.
[53] G. R. Fulmer, A. J. M. Miller, N. H. Sherden, H. E. Gottlieb, A. Nudelman, B. M. Stoltz, J. E. Bercaw, K. I. Goldberg, *Organometallics.* **2010**, *29*, 2176–2179.

Manuscript received: November 1, 2023
Accepted manuscript online: December 13, 2023
Version of record online: December 21, 2023